

Supporting Information

Unstable-Fe-sites induced formation of mesopores in microporous zeolite Y without organic template

Dongdong Guo,^a Baojian Shen,^{*a} Guodong Qi,^b Liang Zhao,^a Jun Xu,^b Feng Deng,^b

Yuchen Qin,^a Qiaoxia Guo,^a Shenyong Ren,^a Xionghou Gao,^c Song Qin,^d Baojie

Wang,^c Hongjuan Zhao,^c Honghai Liu,^c Xinmei Pang^c

Experimental Section

Physicochemical Characterization

Powder X-ray diffraction (XRD) were obtained on a Bruker AXSD8 Advance X-ray diffractometer using nickel-filtered Cu K α X-ray source radiation and operated at 40 kV and 30 mA, the 2 θ angle range was scanned from 5° to 35° at a speed of 2°/min with slit parameters DS = SS = 1° and RS = 0.3 nm; Diffuse reflectance UV-vis spectra were recorded on a Perkin-Elmer Lambda 900 UV/VIS/NIR spectrometer, the powder samples were loaded in a quartz cell, and the spectra were collected at 200 - 700 nm referenced to BaSO₄; UV Raman spectra were recorded with a Jobin-Yvon T6400 triple-stage spectrograph using 244 nm radiation as the exciting source; The bulk chemical compositions were measured by X-ray fluorescence (XRF, Rigaku ZSX 100e); Temperature-programmed desorption of ammonia (NH₃-TPD) profile was recorded in the range of 100 - 550 °C using a heating rate of 10 K/min under pure He flow (1.5 L/h); N₂ isotherms were measured with a Micromeritics ASAP 2020 apparatus at -196 °C, prior to the measurement, the samples were vacuum-degassed at 350 °C for 5 h, the total surface area was determined by the BET method, the *t*-plot method was applied to obtain the micropore volume and external surface area, the pore size distributions were obtained from the desorption branch using the BJH method; TEM was carried out in a JEOL JEM-2100 microscope operated at 200 kV; ESR spectra were measured at X-band (9 GHz) using a JEOL JES-RE1XESR spectrometer, the samples were placed in a quartz tube with an inner diameter of 3 mm and measured at -196 °C; Solid-state NMR spectra were measured at ambient

temperature with a Varian Infinityplus-300 spectrometer at resonance frequencies of 59.584 and 78.1 MHz for ^{29}Si and ^{27}Al , respectively. ^{129}Xe NMR experiments were carried out at 9.4 T on a Varian Infinityplus-400 spectrometer, the resonance frequency is 110.52 MHz for ^{129}Xe , a 10 mm static probe was employed to acquire ^{129}Xe NMR spectra.

Zeolites sample preparation

The hydrothermal synthesis of Fe-NaY was carried out using $\text{Fe}(\text{NO}_3)_3 \cdot 9\text{H}_2\text{O}$ dissolved in water as the iron component to synthesis gels with molar composition $2.45 \text{ Na}_2\text{O} : 1 \text{ Al}_2\text{O}_3 : 8.08 \text{ SiO}_2 : 187.42 \text{ H}_2\text{O} : x \text{ Fe}_2\text{O}_3$, where x is the molar ratio of Fe_2O_3 in the starting gel. Pure NaY was prepared by omitting Fe in the gel.

NaY and Fe-NaY were chosen for further dealumination studies. NH_4^+ -form samples were prepared by ion exchange with NH_4Cl solutions (denoted $\text{NH}_4\text{-Y}$, $\text{NH}_4\text{-Fe-Y}$, respectively). The ion exchange step was performed at 90 °C for 1 h using a solution-to-zeolite ratio of 10 mL/g. The pH of the NH_4Cl solution was adjusted to 3.3 ~ 3.5 with aqueous hydrochloric acid (1 mol/L). After the ion exchange step, the zeolite was thoroughly washed and dried at 120 °C for 12 h. $\text{NH}_4\text{-Y}$ and $\text{NH}_4\text{-Fe-Y}$ zeolites were heated in a quartz tube in 100% steam at 650 °C for 2 h. After 2 hours, the steam supply was stopped, and the steamed zeolites were cooled under air atmosphere. And then, followed a repeated ion exchange and steaming process above. Drying the samples afforded the products, and then we obtained the final products by treatment with solutions of oxalic acid to remove extra-framework Fe. The ultra-stable Y zeolite prepared from the parent NaY was named USY, and the final

products made from the Fe-NaY were nominated USY_{Fe}. In addition, Fe-NaY sample was studied when the second steam treatment temperature decreased by 100 °C (550 °C, 2 h).

Catalytic testing

To assess the differences in catalytic performance of the catalysts, the catalytic cracking of the fresh catalysts was performed with 1,3,5-triisopropylbenzene (TIPB) as the model compound. A flow-type apparatus equipped with a fixed-bed reactor was used. Nitrogen was used as the carrier gas. The USY and USY_{Fe} zeolites were pressed binder-free, crushed, and sieved into particles with a diameter between 0.2 and 0.3 mm. Activation of the catalysts (25 mg) was carried out in situ at 500 °C for 2 h with a nitrogen flow rate of 6 L/h. Nitrogen saturated with TIPB at 90 °C (flow rate = 12 L/h) was passed through the reactor at 170 °C. The reaction products were analyzed online by a gas chromatograph equipped with a flame ionization detector.

Catalytic reaction kinetics was determined in tubular quartz reactors, with a nitrogen flow rate of 12 L/h, and a catalyst weight of 25 mg. Before the reaction, the catalysts were activated in the reactor in flowing nitrogen at 500 °C for 2 h with a heating ramp of 10 °C /min. The reaction temperature was from 120 to 150 °C. The products were analyzed in the effluent gas stream with an on-line Agilent (GC 1790) gas chromatograph with FID detector.

The reaction rate (r_i) was calculated as^{1,2}:

$$r_i = \frac{X_i V}{m_{cat}}$$

Where X_i is the individual reaction conversion, V is the volumetric flow rate of the feed, and m_{cat} is the weight of the catalyst. The apparent activation energy (E_{app})

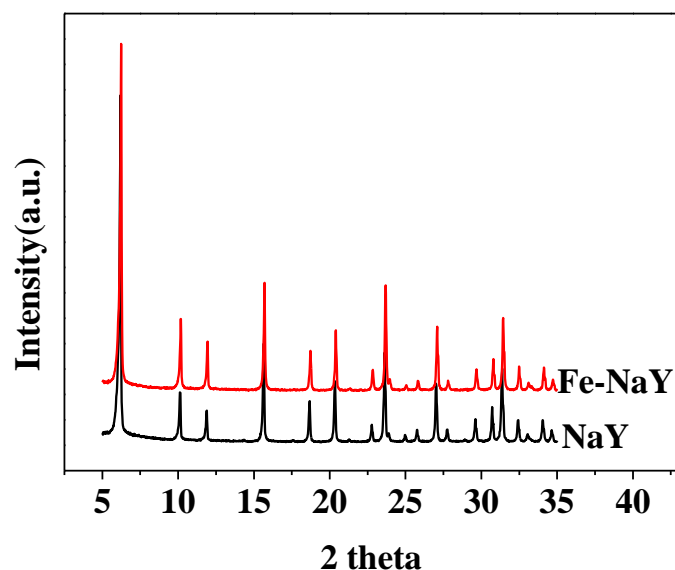
and pre-exponential term (*App.*) are defined as:

$$\ln r = \frac{-E_{app.}}{RT} + \ln App.$$

The apparent activation energies were determined from the slopes of the Arrhenius plots.

Dalian heavy vacuum gas oil was employed as the feedstock for catalytic cracking with an advanced catalyst evaluation unit (ACE, Kayser Technology, USA) operated at 530 °C. The detailed preparation of the aged catalysts were described elsewhere.³

Characterization



Supporting Fig. 1 XRD patterns of NaY and Fe-NaY. Diffraction patterns show that the diffraction lines of (331), (511、333), (440), (533), (642、822), (660), (555、751), (664) at 2θ of ca. 15, 18, 20, 23, 27, 30, 31, 34° indexed to the faujasite regularity of NaY are observed for the Fe-NaY samples. Indicating that the structure of the zeolite remained intact after insertion of iron.

Table S1 Properties of NaY and Iron-Containing Fe-NaY samples

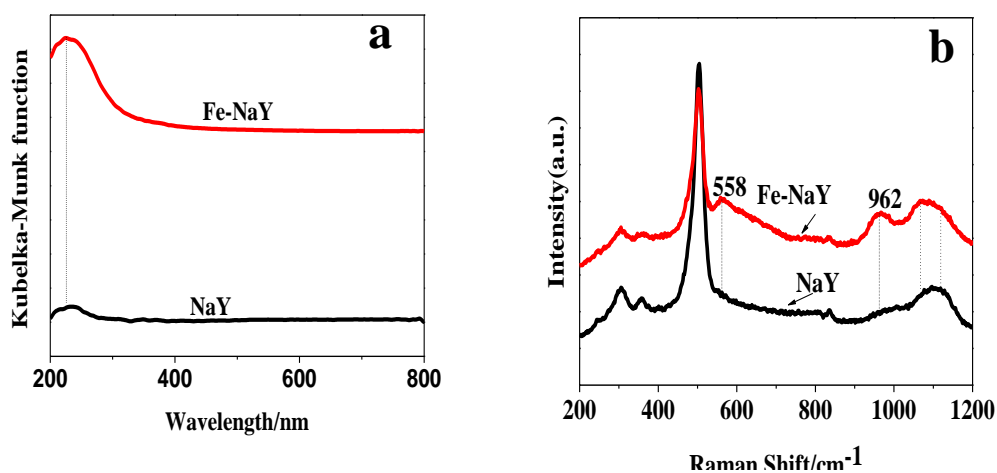
Sample	Fe content in				S_{BET}^c $\text{m}^2 \text{g}^{-1}$	S_{exter}^d $\text{m}^2 \text{g}^{-1}$	V_{pore}^e $\text{cm}^3 \text{g}^{-1}$	V_{micro}^d $\text{cm}^3 \text{g}^{-1}$
	sample ^a (wt. %)	$\text{SiO}_2/\text{Al}_2\text{O}_3^b$	a_0^b/nm	color				
Parent NaY	0.06	5.9	2.461	white	711	26	0.37	0.34
Fe-NaY	0.30	5.7	2.462	white	689	16	0.37	0.34

^a XRF. ^b XRD. ^c BET method. ^{d, e} t -plot.

The results in Table S1 showed that besides silicon and aluminum, iron was the metal element in the NaY sample. The presence of Fe in zeolites was unavoidable due to the precursors used in the conventional preparation of zeolites.⁴ The content of Fe in the NaY sample was at the trace amount level (0.06 wt. %). In the case of Fe-substituted NaY, the unit cell parameter (a_0) increased. The expansion of the unit cell volume is in line with the theoretical expansion based on the difference in the

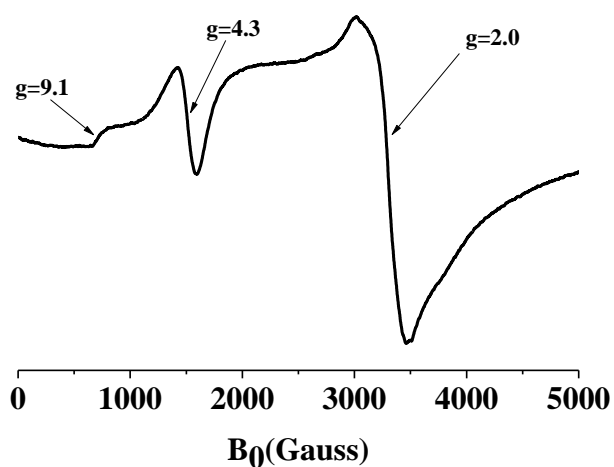
ionic radii of Al^{3+} (0.53 Å) and Fe^{3+} (0.77 Å) as well as the amount of Al^{3+} on framework substituted by Fe^{3+} . On the other hand, the iron cations were probably incorporated in the framework after hydrothermal synthesis. The color of the Fe-NaY samples synthesized in this work was also shown in Table S1 since it was a simple indication whether bulk iron oxide existed.⁵

UV/Vis diffuse reflectance spectra of NaY and Fe-NaY were shown in Supporting Fig.2a. Fe-NaY exhibited a typical absorption band centered at 220 nm, while NaY showed a very weak peak of at 220 nm (because the NaY zeolite contains 0.06 wt. % of Fe, Table S1). The band at 220 nm originated from the ligand-to-metal charge-transfer transition between the Fe and O atoms of Fe-O-Si species in the zeolite framework.^{6,7} Supporting Fig. 2b showed the UV Raman spectra of NaY and Fe-NaY with excitation by the 244-nm line, which was close in energy to the charge-transfer band of Fe-NaY at 220 nm. The UV Raman spectrum of Fe-NaY was different from NaY by the presence of two bands at 558 and 962 cm^{-1} . These bands are assigned to the symmetric and asymmetric stretching vibrations, respectively, of framework Fe-O-Si species.^{6,8} Therefore, the UV Raman results demonstrate that framework Fe is present in the Fe-NaY zeolite sample.

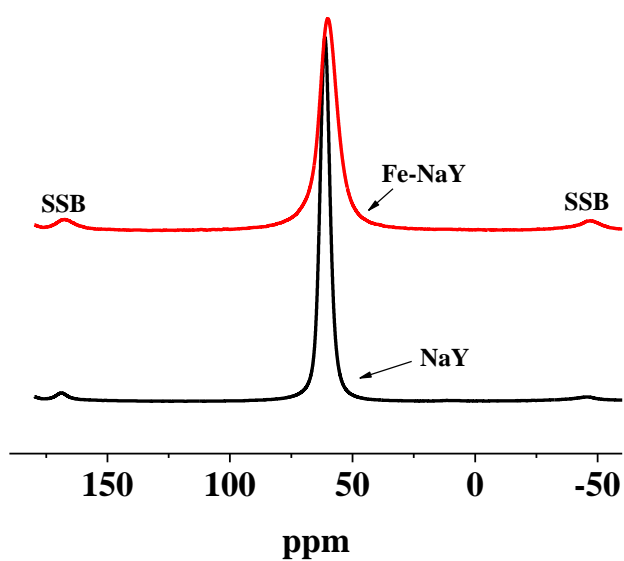


Supporting Fig. 2 a) UV/Vis diffuse reflectance spectra of NaY and Fe-NaY. b) UV resonance Raman spectra of NaY and Fe-NaY with 244 nm excitation.

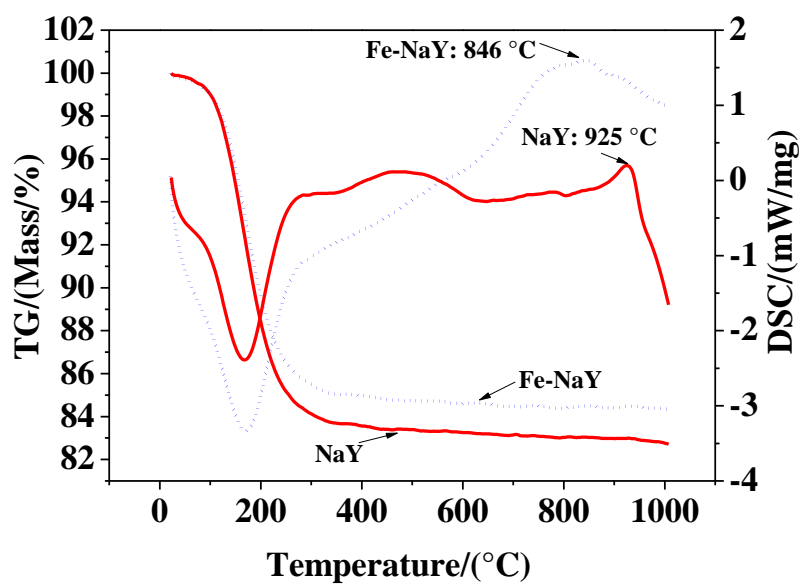
In the ESR spectrum of the parent Fe-NaY sample, three signals, a strong sharp peak at $g = 2.0$ and two other structures at $g = 4.3$ and 9.1 were observable (Supporting Fig.3), which supported the views of Goldfarb et al.⁹ and Liu et al.¹⁰ They suggested that Fe^{3+} in the framework lattice gave a $g = 2.0$ signal. Fe^{3+} has five unpaired electrons in the low-field, high spin state. At lower symmetries, extra-framework Fe^{3+} ions have a distorted tetrahedral symmetry, leading to a $g = 4.3$ line in defect sites in which the Fe^{3+} ions are coordinated to lattice oxygens and to one or two terminal oxygens.^{11,12} The presence of a $g = 9.1$ signal, originating from the lowest Kramers doublet, is characteristic of high-spin Fe^{3+} when $E/D = 1/3$,^{13,14} which may be attributed to Fe^{3+} ions in distorted tetrahedral coordination. We propose that the existence of “unstable Fe^{3+} sites” distorted of framework Al (Fig. S4), which decreased the structural stability. This is consistent with observation by Tatyana and coworkers¹⁵, who found that thermal treatment led to dislocation of framework Fe^{3+} ions from the walls of Fe-MCM-41.



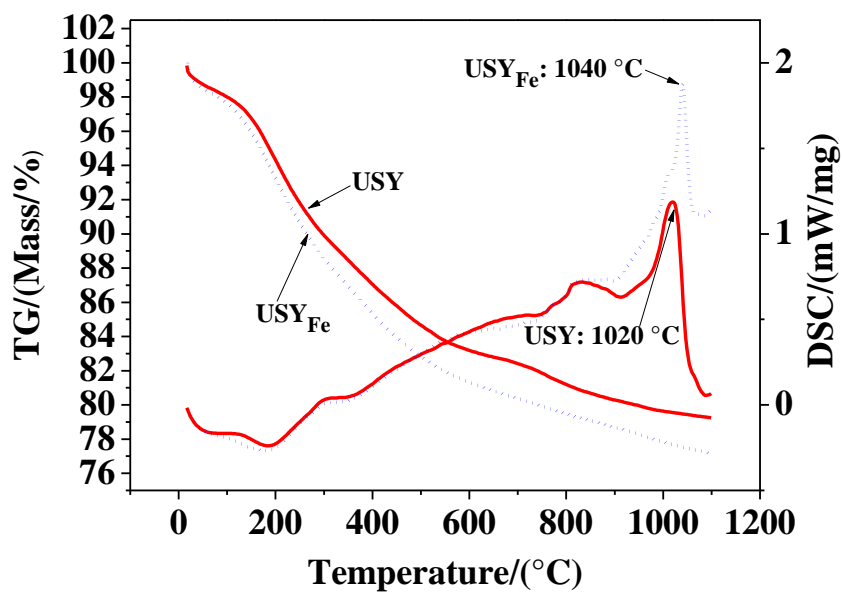
Supporting Fig. 3 X-band ESR spectra of Fe-NaY at $-196\text{ }^{\circ}\text{C}$.



Supporting Fig. 4 ^{27}Al MAS NMR spectra of the NaY and Fe-NaY zeolites.



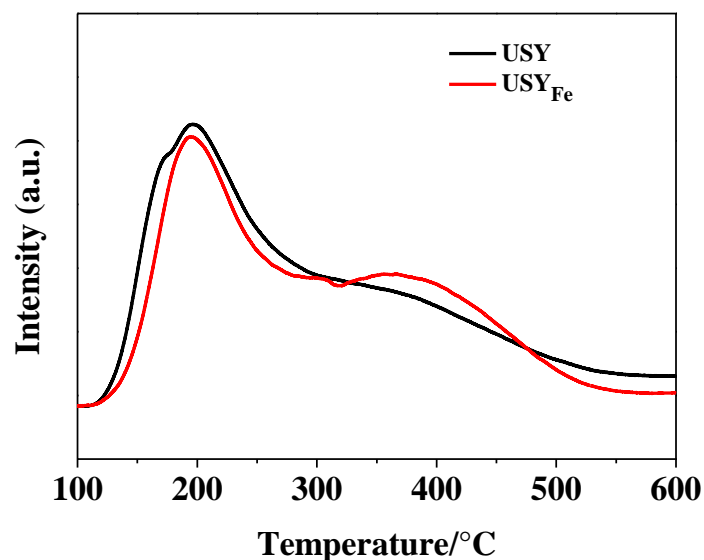
Supporting Fig. 5 The TG/DSC curves of the parent NaY and the Fe-NaY zeolites



Supporting Fig. 6 The TG/DSC curves of the USY and the USY_{Fe} zeolites

Table S2 Acidity measurement by adsorption-desorption of pyridine by IR spectroscopy

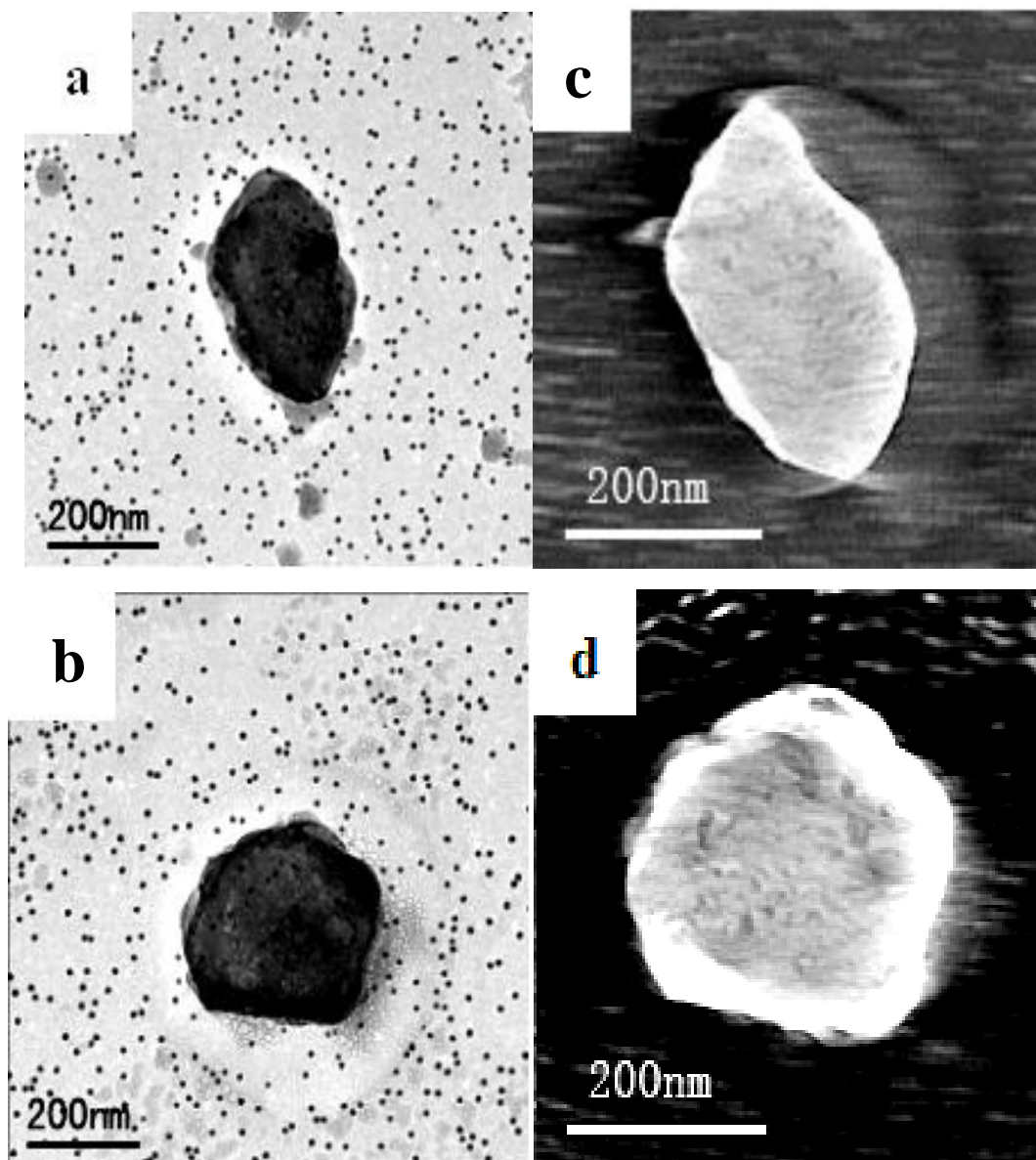
Sample	Amount ($\mu\text{mol g}^{-1}$) and distribution of acid sites			
	Total acid (200°C)		Media and strong acid (350°C)	
	Brønsted	Lewis	Brønsted	Lewis
USY	184	280	62	86
USY _{Fe}	162	272	96	106



Supporting Fig. 7 NH₃-TPD curves of the USY and USY_{Fe} zeolites

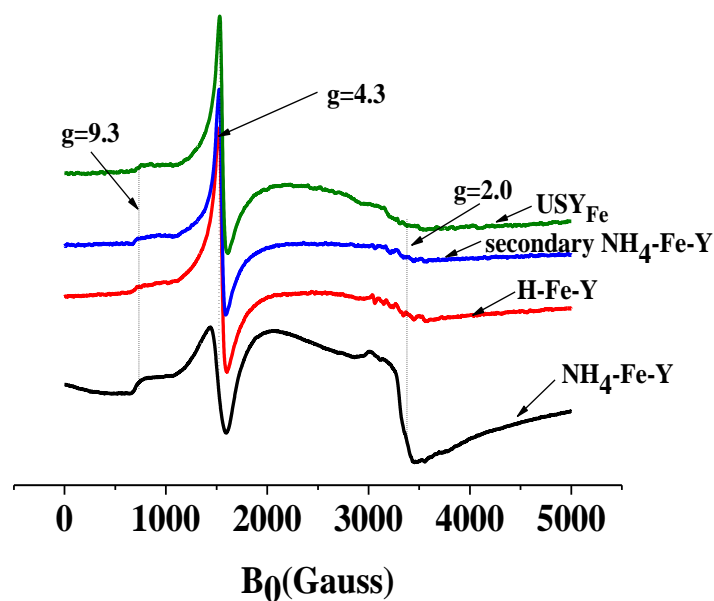
TEM was also a versatile technique to study nanostructured materials. For imaging mesopores in zeolites, however, TEM does not suffice, and electron tomography (ET) based on TEM tilt series was used. 3D reconstructions of zeolite crystals were obtained and analyzed (Supporting Information S8). In the thin slices through the 3D-TEM reconstructions of USY and USY_{Fe} in Fig.S8c and S8d, the mesopores could be distinguished very well as dark gray areas, which coincided with the N₂ sorption results exhibited in text Table 1. The diameters of the mesopores visualized with 3D-TEM were 3-20 nm for USY and 4-40 nm for USY_{Fe}. This is in excellent agreement with the pore-size distributions calculated from the nitrogen desorption isotherms in text Fig.1: 4-20 nm and 4-40 nm for USY and USY_{Fe}, respectively. Analysis of slices of the tomogram revealed that the mesopores of USY_{Fe} are larger than in USY. From detailed studies of two crystals using ET, we believe that the

porosities of zeolite USY_{Fe} crystals are hierarchical in nature, that is, micropores, small mesopores, and large mesopores present in one and the same crystal.



Supporting Fig. 8 Electron microscopy and electron tomography study of USY and USY_{Fe} samples. a) The TEM micrographs of the USY, b) The generation of more-porous structures as can be seen from USY_{Fe} ; The numerical cross-sections through 3D reconstructions of the particles provided by electron tomography clearly depict the presence of mesopores, as well as their interconnectivity and shape: c) 1.08 nm thick slice of USY; d) 0.83 nm thick slice of USY_{Fe} sample.

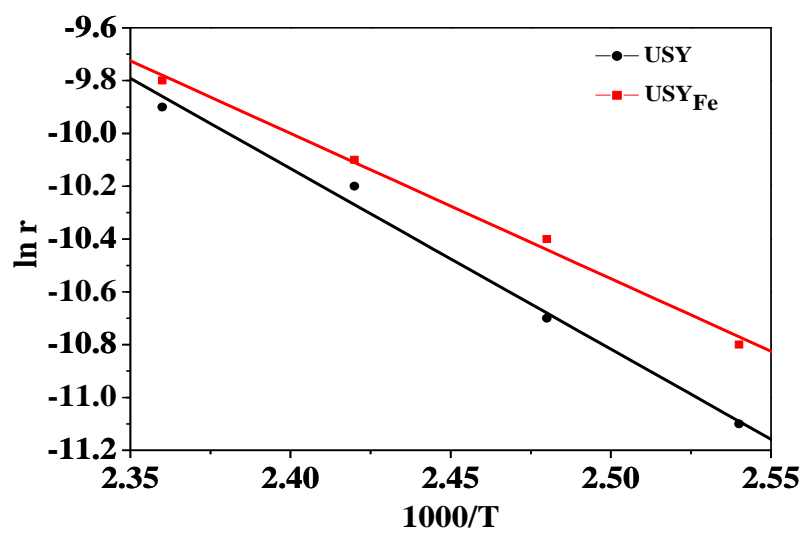
The ESR of $\text{NH}_4\text{-Fe-Y}$ zeolite in Supporting Figure 9 showed that the relative strength of the signal at $g = 2.0$ (which is ascribed to iron species with tetrahedral coordination) decreased and that the $g=4.3$ (ascribed to iron species with defect sites) increased compared with that of Fe-NaY (Supporting Figure 3), suggesting that a few of irons are dislodged from the zeolite framework. Crystallographically, the defect left by the removal of iron is in good agreement with the instability of tetrahedral coordination of the framework Fe^{3+} ions. Meanwhile, the extraction of Si-O-Fe units will inevitably involve the hydrolysis of residual Si-O-Fe and Si-O-Al linkages in the zeolite framework by further treatment. From the ESR results presented in H-Fe-Y, secondary $\text{NH}_4\text{-Fe-Y}$, and USY_{Fe} zeolites, no framework iron could be detected, indicating that almost all of the Fe species exist in form of clustered Fe_2O_3 . The result further suggests that the Fe^{3+} ions are easily dislocated from the framework by steaming to generate structural defects. Apparently, it is difficult for much deferrization-dealumination-generated defect sites to accommodate the $\text{Si}(\text{OH})_4$, which is well accepted as the structural unit for the repair of the iron or aluminum defects in zeolite framework. That means that these defects probably can not be repaired during the steaming treatment.



Supporting Fig. 9 X-band ESR spectra of $\text{NH}_4\text{-Fe-Y}$, H-Fe-Y , secondary $\text{NH}_4\text{-Fe-Y}$ and USY_{Fe} at $-196\text{ }^\circ\text{C}$.

Table S3 The products distribution (wt. %) in the catalytic cracking of Dalian heavy oil.

Items	Catalyst USY	Catalyst USY_{Fe}	Difference value
Dry gas	3.63	3.05	-0.58
Liquefied petroleum gas (LPG)	22.31	20.64	-1.67
Gasoline	37.20	39.68	2.48
Light cycle oil (LCO)	19.96	20.81	0.85
Bottoms	7.39	7.51	0.12
Coke	9.51	8.29	-1.22
Gasoline+LCO	57.16	60.49	3.33



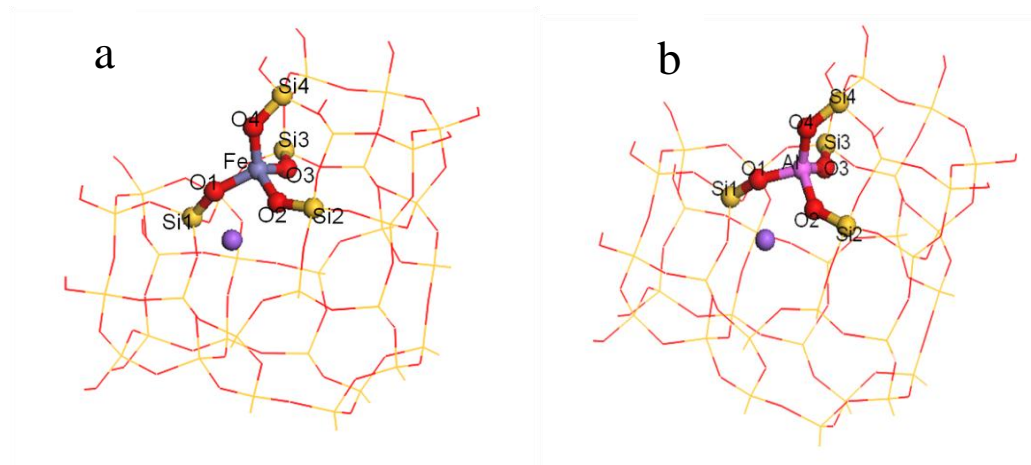
Supporting Fig. 10 Arrhenius plots of monomolecular cracking of TIPB over USY and USY_{Fe} samples.

The computational details

Density Functional Theory (DFT) calculations were performed using the program package Dmol in Materials Studio 5.0^{16,17} of Accelrys, Inc. (Accelrys Inc.; San Diego, CA) The generalized gradient approximation (GGA) using the exchange-correlation functional developed by Perdew and Wang (PW91) was introduced.¹⁸ The localized double-numerical basis set with polarization functions (DNP) was employed, which are more accurate than but comparable in size to the Gaussian basis sets 6-31G (d,p). The tolerances of energy, gradient and displacement convergence were 2×10^{-5} Ha, 0.004 Ha/Å and 0.005 Å, respectively. The self-consistent field (SCF) calculations were carried out with the spin-polarization Kohn-Sham equation. The SCF tolerance was set to 10^{-5} Ha.

In order to substantiate the mechanism reported, the zeolite was represented using the zeolite T36 cluster model composed of 36 tetrahedral atoms of the framework. The Fe-FAU ($\text{FeSi}_{35}\text{O}_{72}\text{NaH}_{24}$) and Al-FAU ($\text{AlSi}_{35}\text{O}_{72}\text{NaH}_{24}$) models were optimized by DFT method. Each model contains of a sodalite cage and two double six-rings. The structures of the models are shown in Figure 11a and 11b. The atoms at the edge of the cluster were terminated by H atoms. The initial coordinates of the zeolite structures were obtained from the data base of Materials Studio 5.0. During the geometry optimization, the coordinates of atoms displayed using balls and sticks were allowed to relax. The coordinates of atoms displayed using lines were frozen. Since there is one type of T site for Fe in the NaY structure, its structure and stability is studied first. The calculated bond lengths and bond angles are listed in Table S3a and

S3b. We found that the bond lengths of Fe-NaY are longer than in NaY, which decreases the thermal stability. Furthermore, the bond angles for Fe-NaY and NaY show a difference, which agrees quite well with the distortion of the structure.



Supporting Fig.11 the cluster mode representing the framework structure of Fe-FAU (a) and Al-FAU (b).

Table S3a Bond lengths.

Fe-FAU	Bond length (Å)	Al-FAU	Bond length (Å)
Fe-O1	1.8595	Al-O1	1.7956
Fe-O2	1.8589	Al-O2	1.8085
Fe-O3	1.8014	Al-O3	1.7325
Fe-O4	1.7877	Al-O4	1.7455
Si1-O1	1.5862	Si1-O1	1.6021
Si2-O2	1.6134	Si2-O2	1.6187
Si3-O3	1.6239	Si3-O3	1.6072
Si4-O4	1.6107	Si4-O4	1.6080

Table S3b Bond angles.

Fe-FAU	Bond angle (deg.)	Al-FAU	Bond angle (deg.)
O1-Fe-O2	101.95	O1-Al-O2	101.78
O2-Fe-O3	107.15	O2-Al-O3	110.78
O3-Fe-O4	113.85	O3-Al-O4	112.92
O1-Fe-O4	113.91	O1-Al-O4	112.83
Fe-O1-Si1	148.40	Al-O1-Si1	149.27
Fe-O2-Si2	139.99	Al-O2-Si2	140.84
Fe-O3-Si3	134.42	Al-O3-Si3	139.75
Fe-O4-Si4	148.40	Al-O4-Si4	133.18

REFERENCES

- [1] T. F. Narbeshuber, H. Vinek and J. A. Lercher, *J. Catal.*, 1995, **298**, 388.
- [2] X. F. Li, B. J. Shen and Ch. M. Xu, *Appl. Catal.A: Gen.*, 2010, **375**, 222.
- [3] Zh. X. Qin, B. J. Shen, Zh. W. Yu, F. Deng, L. Zhao, Sh. G. Zhou, D. L. Yuan, X. H. Gao, B. J. Wang, H. J. Zhao and H. H. Liu, *J. Catal.*, 2013, **298**, 102.
- [4] L. V. Pirutko, V. S. Chernyavsky, A. K. Uriarte and G. I. Panov, *Appl. Catal.A: Gen.*, 2002, **227**, 143.
- [5] P. Ratnasami and R. Kumar, *Catal. Today*, 1991, **9**, 329.
- [6] C. Li, G. Xiong, Q. Xin, J. Liu, P. Ying, Z. Feng, J. Li, W. Yang, Y. Wang, G. Wang, X. Liu, M. Lin, X. Wang and E. Min, *Angew. Chem. Int. Ed.*, 1999, **38**, 2220.
- [7] M. Schwidder, M. S. Kumar, K. Klementiev, M. M. Pöhl, A. Brückner and W. Grünert, *J. Catal.*, 2005, **231**, 314.
- [8] K. J. Sun, F. T. Fan, H. A. Xia, Z. C. Feng, W. X. Li and C. Li, *J. Phys. Chem. C*, 2008, **112**, 16036.
- [9] D. Goldfarb, M. Bernardo, K. G. Strohmaier, D. E. W. Vaughan and H. Thomann, *J. Am. Chem. Soc.*, 1994, **116**, 6344.
- [10] D. Liu, Sh. Bao and Q. Xu, *Appl. Catal.A: General*, 1997, **158**, 93-104.
- [11] P. Ratnasamy and R. Kumar, *Catal. Today*, 1991, **9**, 329.
- [12] J. W. Park and H. Chon, *J. Catal.*, 1992, **133**, 159.
- [13] A. Abragam and B. Bleaney, In *Electron Paramagnetic Resonance of Transition Metal Ions*, Oxford, 1970, pp 156-163.
- [14] J. R. Pilbrow, *Transition Ion Electron Paramagnetic Resonance*, Oxford, 1990, pp 125-144.
- [15] A. Tatyana, Konovalova, Y. L. Gao, L. D. Kispert, J. V. Tol and L. C. Brunel, *J. Phys. Chem. B*, 2003, **107**, 1006.
- [16] B. Delley, *J. Chem. Phys.*, 1990, **92**, 508.
- [17] B. Delley, *J. Chem. Phys.*, 2000, **113**, 7756.
- [18] J. P. Perdew, K. Burke and M. Ernzerhof, *Phys. Rev. Lett.*, 1996, **77**, 3865.